

# Sedimentary, Diagenetic and Accumulation Characteristics of an Offshore Oil-gas Field—a Case Study of Huizhou Depression, Pearl River Mouth Basin, South China Sea

**Longlong Liu**

Lingnan Normal University

**Yinjiao Wu**

Lingnan Normal University

**Hongzhi Dong**

Shandong University of Science and Technology

**Ronghua Fan**

PetroChina Qinghai Oilfield Company

**Zhongqiang Sun** (✉ [sunzhongqiang@lingnan.edu.cn](mailto:sunzhongqiang@lingnan.edu.cn))

Lingnan Normal University

**Rihui Huang**

Lingnan Normal University

**Jinliang Zhang**

Beijing Normal University

---

## Research Article

**Keywords:** sandstones, debris contribute, Mechanical compaction, permeability reservoir

**Posted Date:** December 3rd, 2021

**DOI:** <https://doi.org/10.21203/rs.3.rs-1114529/v1>

**License:**  This work is licensed under a Creative Commons Attribution 4.0 International License. [Read Full License](#)

---

## Abstract

In the Z21 oil-gas field, a total of six depositional lithofacies and two depositional elements were identified based on core observation. Three main diagenetic processes, namely mechanical compaction, cementation, and dissolution of Miocene Zhujiang Formation sandstones were identified according to thin section and scanning electron microscope (SEM) of core samples. Cementations mainly contain silica cementation, carbonate cementation, clay minerals and pyrite. A total of three main pore types, residual primary intergranular pores, secondary dissolution pores and micropores, were identified. Sand sheet deposited in low-energy environment and is characterized by relatively low porosity and permeability values. Larger grain-sized sandstones are of higher quality compared to smaller-sized sandstones. Mechanical compaction, calcite cementation and clay mineral cementation play a key role in reducing porosity and permeability, whereas dissolution of feldspar and debris contribute significantly to improving the reservoir quality. The gas charge occurs prior to oil charge, forming a gas cap in the structural high and an oil ring in the lower formation. Irreducible water stored in the lenticular sandstone of low-porosity and permeability reservoir may convert to movable water as the drill and production perform.

## Introduction

Ocean energy resources play a significant role in national interest and people's livelihood. Development of ocean energy resources not only guarantee our country's energy security, but also reflect the national sustainable capacity<sup>1</sup>. Hydrocarbon resource, as an essential type of ocean energy resources, has been drawing more and more attention in respect of perspective, exploration, exploitation and other respects. According to the results of the national oil and gas resources evaluation, geological reserves of China's offshore oil and gas are  $1.074 \times 10^{10}$ t and  $8.1 \times 10^{12}$ m<sup>3</sup>, respectively<sup>2</sup>. As with the Bohai Bay Basin<sup>3</sup> and the East China Sea Shelf Basin<sup>4</sup>, the Pearl River Mouth Basin (PRMB) in the South China Sea (Figure. 1a) is an agate treasure basin characterized by abundant petroleum resources and other natural resources<sup>5,6</sup>. Huizhou depression, one of the many potential depressions in the PRMB (Figure.1b), has been studied by many geologists in terms of source rock<sup>7</sup>, stratigraphic sequence<sup>8</sup>, depositional system<sup>9-11</sup> and other aspects. Huizhou depression is an important area rich in oil and gas accumulation with a total geological reserve of  $20.87 \times 10^8$ m<sup>3</sup> and a proved reserve of  $6.03 \times 10^8$ m<sup>3</sup><sup>12,13</sup>. The offshore Z21 gas field (Figure. 1b and 1c), discovered in 1990, and is the only one gas field in the Huizhou depression. So far, there are a total of 17 development wells and 3 exploratory wells in the field.

The reservoir connectivity and reservoir quality are two concerned issues for the gas field. The reservoir connectivity of Z21 oil-gas field was discussed in a qualitative sequence-related method by Ding et al.<sup>10</sup> and in a quantitative method by Liu et al.<sup>14</sup>. For the sake of future development and production of the field, it is critical to study the controlling factors on the reservoir quality. This paper aims at studying the sedimentary features and diagenesis processes of Miocene Zhujiang Formation in Z21 oil-gas field and tries to quantitatively analysis the controlling factors on reservoir quality. Meanwhile, petroleum accumulation characteristics were qualitatively analyzed based on reservoir quality study.

The Pearl River Mouth Basin is an underwater extension of the South China continent with a length of about 800km, a width of 100-300 km and an area of 27 km. Its depth varies from dozens of meters to more than 3000 m<sup>15,16</sup>(Figure. 1a and 1b). Huizhou depression lies in the mid-eastern region of PRMB, limited by the North Fault Terrace in the north and Dongsha uplift in the south. Its east and west are Huilu Low uplift and Xi-jiang depression respectively (Figure. 1b). The studied area Z21 oil-gas field lies in the south of Huizhou depression, adjacent to the Dongsha uplift (Figure. 1b). In a structural sense, structural highs are developed in the east and structural lows are in north-west, southwest and northeast (Figure. 1c). Fence diagram from three-dimensional structural model provides a visual perspective to understand the structural feature (Figure. 1c). The target reservoir, K22 layer, lies in the middle of Zhujiang Formation (Figure. 2), is the main production interval of Z21 oil-gas field.

From the Paleocene to Quaternary, the basin contains eight formations: Shenhua (SH), Wenchang (WC), Enping (EP), Zhuhai (ZH), Zhujiang (ZJ), Hanjiang (HJ), Yuehai (YH), and Wanshan (WS), Figure. 2a<sup>14,17,18</sup>. In Huizhou depression, the main sandstone reservoirs are ZH and ZJ formations. In the lower ZJ Formation widely developed a set of carbonate platform, whereas in the middle and upper part of the ZJ Formation, two sets of fine- to medium-grained sandstones were widely deposited, forming the principal reservoir of Huizhou depression (Figure. 2b).

The deposits of ZH Formation, characterized by a thickness range of 500-1100 m, vary from continental delta to marine deltaic<sup>8,19</sup> and also consists of sediments dominated by tides<sup>20</sup>. In terms of stratigraphic sequence, the short-term, middle-term and long-term cycles were studied by scholars such as Cheng et al.<sup>21</sup> and Wei et al.<sup>8</sup>. Based on seismic technology such as root mean square amplitudes, with the

assistance of sedimentology and sequence stratigraphy, favorable areas for prospecting reserves in Huizhou depression were predicted<sup>16,21,22</sup>.

It is a common knowledge that the WC Formation and EP Formation played an essential role in the hydrocarbon accumulation of the Huizhou depression<sup>7,23</sup>. EP Formation are characterized by two thin sets of sandstones in the lower formation and a thick set of dark-colored mudstone in the upper formation (Figure. 2a), which is viewed as the potential source rocks<sup>14,24</sup>. The underlying WC Formation has an unconformable con-tact relationship with EP Formation and its lower strata is dominated by a thick set of semi-deep to deep lacustrine dark gray mudstones (Figure. 2a), which were considered essential source rocks in Huizhou depression<sup>19,22</sup>. In short summary, the dark-colored mudstones of the WC and EP Formations are important source rocks for hydrocarbon ac-cumulations in the Huizhou depression<sup>14</sup>.

## Materials And Methods

Depositional system including depositional lithofacies and elements were analyzed based on sedimentary structure, texture, grain size, rock color, seismic data and strati-graphic characteristics and other preexisting geologic knowledge. A total of 40 representative core samples in the Miocene reservoirs were collected from 5 cored wells in the Huizhou depression. To determine pore types and diagenetic minerals, 20 thin sections were made after each core sample was vacuum impregnated with blue epoxy resin. 20 core samples were used for scanning electron microscope (SEM) to identify diagenetic minerals and pore types, using a HITACHI H600 equipment equipped with a LinkQX-200 energy dispersive spectrometer operating at an accelerating voltage of 20 kV and an emission current of 9000 or 9400 nA. The point-counting method (200-300 points per thin section) was applied to analysis rock constituents such as quartz, feldspar, rock fragment and cements. The XRD were conducted using a Rigaku D/MAX-2400 X-ray diffractometer at the Rock-Mineral Preparation and Analysis Lab of the Institute of Geology and Geophysics, Chinese Academy of Sciences, Beijing, China. The porosity and permeability values are collected from Shenzhen Branch of CNOOC (China National Offshore Oil Corporation).

## Results

**Mineral composition and texture.** The detrital mineralogy of the Miocene Zhujiang sandstones is dominated by quartz (range 60.5-85.9 vol%, average 75.7 vol%), followed by feldspar (range 4.7-24.1 vol%, average 14.5 vol%), and rock fragments (range 4.6-18.6 vol%, average 9.9 vol%) (Table. 1). Therefore, the reservoir sandstones of the Z21 oil-gas field are mainly classified as subarkose and lithic arkose, in the average framework composition of Q<sub>76</sub>F<sub>14</sub>R<sub>10</sub> based on the classification by Folk<sup>25</sup> (Figure. 3).

The Miocene sandstones are composed of grains ranging from 0.1 to 1mm in diameter, with an average of 0.39mm. The sandstones are featured by fine- (accounting for 28.6%) to coarse-grained (accounting for 21.4%) sandstones and dominated by medium-grained sandstones (accounting for 50%). The percentage of poorly-sorting, moderately-sorting and well-sorting sandstones are 23.1%, 28.2% and 48.7%, respectively (Table 1).

Table 1

Summary point-counting data exhibiting the detrital composition of the Miocene Zhujiang Formation in Z21 oil-gas field. AD: average diameter of grains; Q: quartz; F: feldspar; R: rock fragments; Mi: Mica; Qc: silica cementation; Cal: calcite; Daw: dawsonite; Py: pyrite; Φ: measured porosity; K: measured permeability; Pt: thin section porosity; /: without; √: trace.

Well	Depth (m)	AD (mm)	Sorting	Framework composition (%)				Diagenetic minerals				Clay (%)	Φ (%)	K (mD)	Pt (%)
				Q	F	R	Mi	Qc	Cal	Daw	Py				
H3	2702.8	0.4	Poorly	58.0	14.0	7.0	/	√	6.0	/	/	9.0	19.5	43.0	6.0
H3	2582.5	0.2	Well	59.0	6.0	4.0	/	/	18.0	√	1.0	9.0	4.0	46.0	3.0
H3	2582.3	0.3	Moderately	62.0	10.0	10.0	√	0.1	4.8	√	√	5.0	19.6	16.0	8.0
H3	2582.0	0.1	Well	59.0	14.0	8.0	0.5	0.1	10.4	√	/	6.0	5.4	0.4	2.0
H3	2581.5	1.0	Poorly	62.0	10.0	6.0	0.1	/	4.6	/	/	8.0	20.1	7.3	9.0
H3	2581.0	0.4	Moderately	63.0	12.0	4.0	√	/	5.1	/	√	6.0	14.3	6.2	10.0
H3	2579.9	0.5	Poorly	60.0	11.0	5.0	1.0	0.5	8.5	2.0	/	5.0	19.0	14.0	7.0
H1	2567.5	0.4	Well	54.0	10.0	6.0	√	√	25.0	/	1.0	/	/	/	4.0
H1	2554.7	0.2	Well	41.0	7.0	3.0	√	/	45.0	/	1.0	/	/	/	3.0
H1	2553.3	0.1	Well	70.0	7.0	7.0	2.0	√	/	/	/	13.0	/	/	2.0
H1	2551.8	0.2	Moderately	66.0	8.0	7.0	2.0	/	1.0	/	1.0	13.0	/	/	2.0
H1	2525.6	0.3	Well	52.0	18.0	16.0	3.0	0.1	/	/		6.0	/	/	5.0
H1	2524.1	0.3	Well	74.0	9.0	9.0	3.0	0.5	/	/	0.5	4.0	/	/	1.0
H1	2523.5	1.0	Well	69.0	4.0	12.0	1.0	/	/	/	/	4.0	/	/	10.0
H1	2521.5	0.3	Moderately	67.0	7.0	4.0	3.0	√	/	/	/	4.0	/	/	1.0
H1	2520.8	0.5	Moderately	52.0	20.0	13.0	0.1	1.0	1.0	/	1.0	6.0	/	/	6.0
H1	2520.2	0.4	Well	56.0	21.0	11.0	√	√	0.5	0.5	2.0	2.0	/	/	7.0
H1	2519.9	0.2	Poorly	75.0	10.0	10.0	√	/	1.0	√	1.0	2.0	/	/	1.0
H1	2519.8	0.3	Well	72.0	6.0	17.0	1.0	/	/	/	/	2.0	/	/	2.0
H1	2519.7	0.3	Well	64.0	15.0	7.0	0.3	√	√	0.5	√	6.0	/	/	7.0
Well	Depth (m)	A.D (mm)	Sorting	Framework composition (%)				Diagenetic minerals				Clay (%)	Φ (%)	K (mD)	Pt (%)
				Q	F	R	Mi	Qc	Cal	Daw	Py				
H1	2518.8	1.0	Poorly	71.0	12.0	4.0	0.1	/	2.0	1.0	√	2.0	/	/	8.0
H1	2518.5	0.5	Well	67.0	11.0	7.0	1.0	√	/	/	/	3.0	/	/	11.0
H1	2518.2	0.5	Moderately	61.0	13.0	10.0	2.0	/	1.0	√	1.0	3.0	/	/	9.0
H1	2517.3	0.5	Moderately	55.0	18.0	10.0	2.0	√	/	/	√	5.0	/	/	10.0
H1	2517.1	0.2	Well	60.0	14.0	7.0	3.0	/	2.0	√	/	9.0	/	/	5.0
H1	2516.8	0.2	Well	55.0	20.0	8.0	2.0	√	1.0	/	1.0	8.0	/	/	5.0
H1	2516.4	1.0	Moderately	70.0	10.0	11.0	1.0	0.5	/	0.5	/	1.0	/	/	6.0
H1	2515.8	0.5	Poorly	67.0	13.0	7.0	1.0	/	1.0	√	1.0	1.0	/	/	9.0
H1	2515.6	0.4	Well	68.0	11.0	6.0	1.0	√	1.0	/	/	2.0	/	/	11.0
H1	2515.1	0.3	Moderately	63.0	12.0	8.0	1.0	/	1.0	/	1.0	3.0	/	/	11.0

Well	Depth (m)	AD (mm)	Sorting	Framework composition (%)				Diagenetic minerals				Clay (%)	$\phi$ (%)	K (mD)	Pt (%)
				Q	F	R	Mi	Qc	Cal	Daw	Py				
H1	2515.0	0.6	Well	66.0	11.0	8.5	1.0	/	2.0	/	0.5	3.0	/	/	8.0
H1	2519.6	0.5	Poorly	56.0	16.0	10.0	3.0	/	1.0	1.0	/	4.0	/	/	9.0
H1	2519.3	0.4	Poorly	59.0	15.0	7.0	2.0	/	2.0	/	1.0	4.0	/	/	10.0
H2	2436.6	0.6	Moderately	61.0	11.0	9.0	/	0.0	1.8	0.5	1.0	3.0	20.8	210.2	13.0
H2	2433.8	0.3	Well	49.0	8.0	3.0	✓	0.5	25.4	1.0	✓	12.0	3.4	0.0	1.0
H2	2431.7	0.5	Moderately	58.0	10.0	8.0	0.5	/	12.5	/	1.0	10.0	10.8	0.2	6.0
H2	2429.7	0.1	Well	59.0	11.0	10.0	/	/	12.0	/	/	6.0	7.6	1.4	2.0
H6-1	2039.9	0.1	Well	60.0	12.0	10.0	0.5	✓	0.5	2.0	1.0	4.0	18.0	186.0	10.0
H6-1	2036.5	0.4	Poorly	62.0	13.0	9.0	1.5	/	0.5	/	/	2.0	13.4	230.0	12.0

### Depositional System

- Lithofacies.** Deposits of Z21 oil-gas field were considered as sand ridges distributed far away from the delta front, dominated by wave and shore current (Figure. 4), which is consistent with previous studies<sup>11,14</sup>. A total of 6 depositional lithofacies were identified (Figure. 5), namely massive fine- to medium-grained sandstone (Sm, Figure. 5-A), ripple cross-laminated fine-grained sandstone (Sr, Figure. 5-B), parallel laminated siltstone and claystone (Fl, Figure. 5-C), lenticular siltstone (Sl, Figure. 5-D), parallel-bedded fine-grained sandstone (Sp, Figure. 5-E), wavy laminated siltstone (Sw, Figure.5-F). Brief descriptions of these six lithofacies are given as follows.

1. Massive fine- to medium-grained sandstone (Sm). This facies is generally fine- to medium-grained, 1 to 3 meters in thickness, light gray in color (Figure. 5-A). This facies is tight, well-sorted, and siliceous cemented, slightly calcareous and occasionally embedded by vertical burrows or tiny muddy strips (Figure. 5-A). This facies is interpreted as the de-positions rapidly formed during the establishment of offshore sandbars in current and wave energies<sup>26</sup>.

2. Ripple cross-laminated fine-grained sandstone (Sr). This facies are usually found within a short interval (less than 0.5m). Obvious soft sediment deformation structures are occasionally observed in this facies. Isolated ferric concretions are occasionally observed within this face (Figure. 5-B). In places, small-scale burrows are developed. This lithofacies is interpreted as the migration of ripples in fluctuating currents, indicating lower flow re-gime<sup>27,28</sup>.

3. Parallel laminated siltstone and claystone (Fl). This facies consists of laminated siltstone or “colorful” claystone units interbedded with millimeter-thick siltstone lamina-tions (Figure. 5-C). Both the upper contact and the lower contact with facies Sm, Sw or Sl are sharp (Figure. 5). Common structures include vertical and lateral bioturbations, calcareous concretions and iron nodules. The fresh surfaces of the interlaminated siltstone are off white in most instances, whereas it's light red or brown on the weathered surfaces.

4. Lenticular siltstone (Sl). This lithofacies make up a large proportion of the cores from K22 set. Figure. 5-D shows the typical lenticular siltstone facies in cores from well H2. Depositional structures within this facies are “messy”, including wavy beddings, flaser beddings, small-scale ripple beddings and lenticular beddings (Figure. 5-D). Shapes of the individual lenticular siltstone bodies are quite different, and the inside of the lenticular bodies are commonly sparsely filled with tiny muddy ripple laminations (Figure. 5-D). Decimeter-thick wavy strips, brown or light brown in color, are commonly interstratified within this lithofacies. Lenticular siltstone generally is related to the transformation of delta front bedforms which benefited by continuous or intermittent waves and coastal currents<sup>29,30</sup>.

5. Parallel-bedded fine-grained sandstone (Sp). Most of this facies is approximately horizontally bedded, with thin muddy laminations interbedded in a random unequal separation distance (Figure. 5-E). This facies is several centimeters to 1.5m, light gray or silver gray in color. In many instances, clear parting lineation are observed in cores and muddy laminations expanded because of absorbing the

moisture. In places yellowish-brown laminations rich of ferric ions are developed within this facies. This lithofacies is interpreted to represent high sedimentation fall-out rates during the gap between the rise and fall of the waves<sup>11,30</sup>.

6. Wavy laminated siltstone (Sw). This lithofacies accounts for a small proportion of all the lithofacies. It's characterized by thin thickness (less than 0.2m) and poor continuity due to the interruption of other lithofacies (e.g., Sr or Sp). Isolated calcareous concretions or 0.01m or thinner laminations rich of iron material are occasionally developed (Figure. 5-F). In general, both the crests and troughs of the waves are relatively gentle (Figure. 5-F)

- **Depositional elements.** Two primary depositional elements characterize the K22 set interval: nearshore sand bar (SB) and sand sheet (SS). Identification of these two elements is mainly based on litho-facies, sedimentary structures, and sequences. Description and interpretation of the two elements are briefly discussed below.

1. Depositional element SB. As shown in Figure. 4, element SB varies from 1.5–5m in thickness with multiple facies association. The sandstone: mudstone ratio is high, and the continuity of SB is generally interrupted by thin units of facies Fl or Sl. Both the upper and lower contact with facies Fl and Sl are gradual or/and sharp. In many places, especially within K22A layer, massive sandstone of SB is well developed (Figure. 5). It's common that isolated iron concretions, ellipse, sphere, bamboo or finger-shaped, are developed within this element. In places, severely rip-up muddy chips are dispersedly distributed within the silty facies Sm. Bioturbation is occasionally found within facies Sw, Sl or Fl in this succession.

Element SB represent the deposits of delta front bedform, which is modified by waves and currents<sup>11</sup>. In this paper, recognition of SB in the plane with the assistance of seis-mic data (Figure. 4) is accordant with predecessors' works<sup>8,10,31</sup>. As shown in Figure. 3, the west and southwest area of the study area, marked by three zones, namely I, II and III, have been widely acknowledged as delta front depositional system, whereas the main zone of Z21 field is involved in the sand ridges which are distributed far away from the delta lobe<sup>10,32</sup>. As the delta front was thrust toward sea basin, the preexisting coarse-grained deposits are continuously transported away from the prodelta zone by the force of wave and then resettle down. If the sediment supply is sufficient, the resettled sandy deposits will be transported again for a certain distance and settle down until the wave force vanishes<sup>14</sup>. The accumulation of the reworked deposits forms a series of sand ridges which are approximately parallel to the shoreline<sup>14</sup>. The amplitude of SB is high and obviously stripped with an NNE trending (Figure. 4).

2. Depositional element SS. SS element is characterized by less than 1m thick individual set of argillaceous silt-stones interbedded with mudstone (Figure. 5). Facies Fl and Sl are well developed within this succession with abundant burrows. Iron concretions of different shapes are also occasionally found in facies Fl and Sl. Other sedimentary structures include small-scale ripple laminates, soft deformation structures and calcareous concretions are observed in places. In general, SS element is dominated by muddy deposits with a high mudstone: sandstone ratio.

SS is interpreted as the result of transferring and reconstructing of the large delta front bedform by wave and coastal current<sup>11,33</sup>. According to the amplitude slice of K22 set, amplitude of the SS is relatively low, and its geometry is sheet-like (Figure. 4). Within SS, the flow energy changes frequently, resulted in various sedimentary structures (Figure. 5). According to seismic inversion slice of K22 set, the west reservoir of well H18 could be classified as a SS depositional zone, whereas well H18 is possibly distributed at the margin of SB or within SS (Figure. 4).

**Pore classification and physical properties.** According to the classification by Schmidt and McDonald<sup>33</sup>, based on the study of thin section and SEM images, a total of three types of pores, namely residual primary intergranular pores (Figure.6a and 6b), secondary dissolution pores (Figure.6a and 6b), and micropores (Figure.6c and 6d), are distinguished in the Miocene reservoir sandstones.

Results of point counting of the thin sections showing residual primary intergranular pores accounting for 82.5% of the total pores, indicating that the pores of the Miocene sandstones in the ZJ Formation are dominated by this pore type. Through observation, the residual primary intergranular pores mainly occur in the condition that there are rare or no cement or matrix blocking the space between detrital grains (Figure.6a and 6b). The secondary dissolution pores are further classified into intragranular pores (Figure. 6a) and intergranular dissolution pores (Figure.6b, moldic pores). The former generally were produced by incomplete dissolution of unstable grains such as feldspar and debris, whereas the latter were mainly generated from dissolution of the edge of detrital grains. The moldic pores were results of complete dissolution of detrital grains (Figure. 6b). There are two kinds of micropores developed within ZJ Formation: micro-fractures (Figure. 6c) and intercrystalline micropores (Figure. 6d). The micro-fractures are mostly observed within the

intervals within directionally arranged grains (Figure. 6c), whereas the intercrystalline micropores are mainly developed within intervals of illitic clays (Figure. 6d).

The porosity values of target formation vary from 10.1–20.1%, with a mean value of 13.9%. The minimum permeability value is 0.2mD, the maximum value is 230mD and the average value is 35.8mD. The porosity and permeability values are characterized by positive linear relationship (Figure. 7a). The Lorenz plot of permeability in Figure. 7b aims to describe the reservoir heterogeneity. For a homogeneous reservoir, the Lorenz plot is characterized by a straight-line AC, unlike a heterogeneous reservoir<sup>35,36</sup>. The Lorenz plot of permeability for the Z21 oil-gas field is an arc between a 0-75.21% of cumulative probability of rock sample range, indicating strong reservoir heterogeneity.

### Diagenesis And Diagenetic Mineralogy

- **Compaction.** Sandstone of K22 layer underwent mechanical compaction progress, as indicated by oriented-arrangement grains (Figure. 8a) and deformed mica (Figure. 8b). Indications for chemical compaction such as sutured contacts are rare in this study interval.
- **Cementation.** In K22 sandstone, cementation minerals mainly include siliceous cements, clay minerals and carbonate cements. Siliceous cements are dominated by authigenic quartz, which are commonly found in the intergranular pores, adjacent to unstable grains like feldspar (Figure.8c). In some cases, quartz overgrowth is observed.

The clay minerals are dominated by kaolinite, appearing as stacked booklets or vermiciform aggregates (Figure. 8d). They are usually found distributed in the residual primary intergranular pores, incompletely filled by other cements such as calcite cements (Figure. 8d). Fibrous (Figure. 8e) or honeycomb-like with spiny terminations (Figure. 6d) illite is also abundant in the target sandstones. Stochastically Oriented-platelet shaped chlorites mostly occur at the rim of grains (Figure. 8f). The relative content of kaolinite, illite and chlorite have a range of 0-82%, 0-55%, and 0-68%, respectively.

Calcite is most widely distributed carbonate cements in the Miocene Zhujiang Formation sandstones. In thin sections, calcite completely plugging the intergranular pores are occasionally observed (Figure. 8g). However, in most cases, calcite cements partially fill the intergranular pores (Figure. 8d). The fibrous dawsonite aggregates are occasionally observed filling the intergranular pores (Figure. 8h).

Pyrite, as minor cements, usually occur in the form of frambooidal aggregates (Figure. 8i). Point-counting analysis shows pyrite has a volume percentage from trace to 4.2%, averaging 1.2%.

- **Dissolution.** Feldspar (Figure. 8j) and rock fragment (Figure. 6a and 6b) dissolution are the main factor attributed to secondary pores. The photomicrographs of the thin sections exhibit that feldspar is partially dissolved along the cleavage planes and fracture surfaces, leaving behind secondary intragranular pores (Figure. 6a). In some intensely dissolved intervals, moldic pores caused by dissolution of rock fragments are observed (Figure. 6b).

## Discussion

**Diagenetic history.** Diagenetic history of the Miocene ZJ Formation sandstones is analyzed according to the types of diagenetic processes, cements, pore types and physical properties and other aspects<sup>37,38</sup>. Based on thin section and SEM observation, the diagenetic processes of studied interval consist of mechanical compaction; quartz; carbonate and clay mineral cementation; pyrite and dissolution. According to Morad et al.<sup>38</sup>, the diagenetic processes can be divided into eodiagenesis and mesodiagenesis. Eodiagenesis in this area is characterized by sediments underwent a paleogeotemperature of approximately 70°C, generally occurs at a depth less than 2 km. As the burying goes on, the diagenetic process comes to mesodiagenesis<sup>38</sup>. Based on reconstruction of burial-thermal history of well H1 in Z21 oil-gas field by Wu<sup>39</sup>, it is found the target ZJ Formation sandstones (mainly 2-3 km) has a corresponding formation temperature of 85-120°C (Figure. 9), illustrating that mesodiagenetic processes occurred.

Mechanical compaction is the bulk volume reduction result from lithostatic stress, characterized by reorientation of framework grains (Figure. 8a), deformation of ductile grains (Figure. 8b) or local fracture of brittle grains (Figure. 6c). Mechanical compaction occurs simultaneously with sediment deposition and is considered to dominate under temperatures ranging from 70°C to 80°C<sup>40</sup>, mainly corresponding to the eodiagenetic stage. No chemical compaction is observed in the microscope.

Quartz cementation occurs in the eodiagenetic process, mainly in the form of authigenic quartz. Mesodiagenetic quartz cementation in sandstones is often ascribed to intra-formational dissolution of detrital silicate phase, due to the low aqueous solubility of SiO<sub>2</sub><sup>41</sup>.

However, there is minimal pressure dissolution of detrital quartz in the ZJ Formation sandstones, proved by no observation of detrital quartz dissolution in the view of thin section and SEM. the typical temperature of chlorite formation is approximately 60–70°C<sup>42</sup>, which refers to the end of the eodiagenetic stage. The photomicrographs of the SEM show that quartz overgrowth coated by authigenic chlorites indicate that authigenic chlorites occur after quartz overgrowth. The terminal of quartz overgrowth is restricted by the occurrence of pyrite (Figure. 8i), indicating that pyrite occurs prior to quartz overgrowth. Feldspar dissolution is considered as important material resources for quartz, kaolinite and illite precipitation<sup>43</sup>, therefore, it is inferred that quartz, kaolinite and illite cementations occur penecontemporaneously or kaolinite occur a little bit earlier than quartz cementations. In acidic conditions, the extensive illitization is associated with a temperature of 140°C<sup>44</sup>, indicating that illite occurs from the eodiagenetic stage, but is mainly formed in the mesodiagenetic stage.

The early calcite completely fills the intergranular pores, and the irregular shape of the calcite indicates it is formed prior or contemporary with severe mechanical compaction (Figure. 8g). In some cases, calcite together with other clay minerals such as kaolinite, usually partially fill the interparticle pores (Figure. 8d). Illite and kaolinite grow on the surface of calcite cementations, indicating that calcite precipitation occurs prior to both illite and kaolinite (Figure. 8d). Another kind of carbonate cementation, dawsonite, is considered as an indicator of CO<sub>2</sub><sup>45,46</sup>. CO<sub>2</sub> stored in the ZJ Formation sandstones derived from both magmatism and organic matter evolution<sup>47</sup>. The acidic fluid, formed due to the CO<sub>2</sub> injection into the sandstones, dissolve unstable minerals such as feldspar or rock fragment grains, producing sufficient Na<sup>+</sup> and Al<sup>3+</sup> for the dawsonite precipitations<sup>48,49</sup>. Therefore, dawsonite precipitations occur after dissolution (Figure. 9).

### Diagenetic Controls On Reservoir Quality

- **Sedimentary facies controls on reservoir quality.** As mentioned above, deposits of H21 gas field were located far away from the delta front which is characterized by complex hydrodynamic conditions<sup>10</sup>, reflected by variable sedimentary structures (Figure. 5). Linking the heterogeneous porosity and permeability values (Figure. 7) to the varying lithofacies types, it is preliminarily inferred that reservoir quality of H21 gas field was significantly affected by depositional settings. As shown in Figure. 10a, statistics of different depositional elements show that both porosity and permeability values of SB are generally higher than those of SS. The SS depositional element is interpreted as sandstones deposited in low-energy environment, poorly sorted and with high matrix content<sup>51</sup>.
- **Grain size controls on reservoir quality.** Another factor affecting the reservoir quality is grain size. The grain size which reflects the primary texture of sandstones, may control the extent of the subsequent diagenetic events<sup>52</sup>. Statistics show that different grain-sized sandstones, namely fine-grained, medium-grained, and coarse-grained sandstone have different porosity and permeability distribution centers (Figure. 10b). As the grain sizes increase, the porosity and permeability values generally become bigger (Figure. 10b). Compared to the smaller-sized sandstones, the larger-sized sandstones are usually well sorted with less matrix grains; meanwhile, rigid framework grains such as quartz are less influenced from complex compaction processes if they are larger-sized<sup>53</sup>.
- **Diagenetic controls on reservoir quality.**

**1. Mechanical compaction.** Mechanical compaction, intergranular pressure solution, cementation, framework grain dissolution, and cement dissolution have all been documented as playing significant roles in modifying porosity of various sandstones<sup>54</sup>. In the Miocene ZJ Formation sandstones, mechanical compaction is characterized by directional arrangement of grains, concave-conves contacts between the grains and plastic deformation of ductile grains. Upon burial, sediments will compact mechanically when the effective stress due to over-burden is increased, so that the porosity and the total rock volume are reduced<sup>55</sup>. As a result of increasing effective stress from the overlying strata during burial, the effect of mechanical compaction increases with the increase of burial depth in eodiagenesis<sup>56</sup>. As shown in Figure.11, as the burial depth goes deeper from approximately 2530-2570 m and from 2585 m to 2620 m, both the porosity and permeability decreases with the depth. Why the porosity and permeability values increase as the reservoir goes deeper in the 2570-2585 m interval? Probably it can be ascribed to two main aspects. Firstly, there is no sufficient sample data related to this depth range. Secondly, at burial depths greater than about 2 km (>70–80°C) quartz precipitation on clastic grains (Figure. 8f) gradually produces a framework of quartz overgrowths which are strong enough to prevent further mechanical compaction<sup>55</sup>; and dissolution of feldspar enhance the porosity volume, indicated by Figure. 8j.

**2. Cementation.** Carbonate cements in this area are dominated by calcite. Dawsonite is ignored for quantitative statistical analysis due to limited samples encountering dawsonite cements. Calcite partially (Figure. 8d) or completely (Figure. 8g) filled intergranular pores, both reducing the pore spaces. As shown in Figure. 11, in general, both porosity and permeability values decrease as the increasing of calcite content, showing a remarkable negative relationship with R<sup>2</sup>=0.7449. However, it is noticed that when the content of calcite is less than

9%, there is no remarkable negative correlation between porosity and calcite (Figure. 12a). The sample that has a relatively higher calcite content of 18% with a permeability value of 48 mD (Figure. 12b) and a porosity value of 4% (Figure. 12a), is interpreted by the development of micro-fracture (Figure. 6c).

Typically, authigenic kaolinite, illite or other clay mineral may be found in nearby primary or secondary pores<sup>57</sup>. Precipitation of kaolinite can only occur when the K<sup>+</sup>/H<sup>+</sup> ratio and silica concentration in the pore water are below certain values and such low K<sup>+</sup>/H<sup>+</sup> ratios are normally only found in fresh or brackish water<sup>58</sup>. That means in intervals where CO<sub>2</sub> concentration is high and dissolution of feldspar and debris is severe, the relative content of kaolinite precipitation could reach as high as 82% (Table. 2). However, the intercrystalline micropores within kaolinite aggregates is poorly developed. Therefore, the more kaolinites are, the more pore spaces were filled, showing a negative correlation between kaolinite and reservoir physical properties (Figure. 13a and 13b). As for illite, intercrystalline micropores within illite aggregates are generally well developed (Figure. 5d), the porosity and permeability values increase as the content of illites increase (Figure. 13c and 13d). However, the convert from illite to the mixed layers of illite and smectite reduces some of pore spaces (Figure. 8e). At another hand, the pore filling illite aggregates may occupy some of pore spaces and result in a decrease in porosity and permeability (Figure. 13c and 13d).

Grain-coating chlorites are generally considered as the porosity-preserving components in the sandstones<sup>42,51,58</sup>. Within ZJ Formation, as shown in Figure. 13e, the porosity increases and then decreases slightly, implying the chlorites coatings may retard quartz overgrowth within a limited content range (Figure. 8f). The relationship between chlorites and permeability is like that between chlorites and porosity (Figure. 13f). As the volume of chlorites accumulate, the porosity and permeability values decrease slightly due to the plugging of pore-filling chlorite aggregates.

In this studied area, although a single type of clay mineral may enhance the reservoir physical properties and another may weaken the congeneric properties, the porosity and permeability still display a decreasing trend with the total clay minerals, with low R<sup>2</sup> values (0.25 and 0.5206, respectively) (Figure. 13g and 13h), indicating that clay mineral cementation is an important control factor of reservoir quality in the area.

Table 2

Relative content of the clay minerals via XRD and the porosity and permeability of the selected samples. K: kaolinite; I: illite; I/S: mixed layers of illite and smectite; C: chlorite; Φ: measured porosity; K: measured permeability.

Well	Depth(m)	Total clay (%)	Relative content of clay minerals (%)				Φ (%)	K (mD)
			K	I	I/S	C		
H3	2581	6	60	0	40	0	14.30	6.20
H3	2581.5	8	40	10	20	30	20.10	7.30
H3	2582	6	82	0	18	0	5.40	0.40
H3	2582.3	5	46	54	0	0	19.60	16.00
H3	2582.5	9	0	0	55	45	4.00	46.00
H3	2579.9	5	19	0	13	68	19.00	14.00
H3	2702.8	9	41	41	15	3	19.50	43.00
H2	2429.7	6	46	17	16	21	7.60	1.40
H2	2431.7	10	17	68	8	7	10.80	0.20
H2	2436.6	3	18	29	27	26	20.80	210.20
H2	2433.8	12	71	17	8	4	3.40	0.03
H6-1	2036.54	2	16	13	34	37	13.40	230.00
H6-1	2039.9	4	12	9	24	55	18.00	186.00

**3. Dissolution.** Dissolution is generally considered as a constructive factor that enhance reservoir quality<sup>51,57,58</sup>. The secondary dissolution pores are dominated by dissolution of feldspar and debris, and therefore, it is meaningful to ascertain whether dissolution is

responsible for the deeper sandstones but with higher porosity and permeability values. The types of pores reflected by thin sections were analyzed by point counting and it is found that the deeper sandstones with higher porosity and permeability values usually have a greater proportion in secondary dissolution pores, whereas the shallower sandstones are dominated by residual primary intergranular pores, which are limited in bulk volume (Figure. 14). Although influence of dissolution on reservoir quality studied in this way is not that rigorous, to some extent, dissolution enhancing the porosity and permeability is still proved in a qualitative way.

**Distribution pattern of water, oil and gas in Z21 structure.** Sources of oil and gas in the Z21 structure in Huizhou Depression has been studied by Zhu et al.<sup>16,50</sup>. The Z21 oil-gas field are characterized by multiple sources. Both the condensate gas in gas reservoir and solution gas in oil reservoir in the upper ZJ Formation are from the same source rocks of EP and WC Formation in HZ21 subsag, which are deposited in shallow lacustrine to swamp, whereas the black oil in the lower ZJ Formation is from semi-deep to deep lacustrine source rocks with significant terrigenous parent organic matters in HZ26 subsag<sup>16</sup> (Figure. 15). The gas reservoir formed earlier than that of oil reservoir in Z21 structure<sup>16</sup>. In 2014, modular formation dynamics test (MDT) was conducted in K22 set of well H1DSa and pure oil samples were collected; however, the subsequent drill stem test (DST) detected water show (not water from mud filtrate caused by drilling engineering) in the same depth of well H1DSa (location see Figure. 4)<sup>16</sup>. More interestingly, oil samples were collected in the depth lower than the interval where MDT and DST were conducted. Whether the main zone is a gas cap and the main zone is an oil ring confuse us. This problem may not be solved unless the source of collected water samples was ascertained. Zhu et al. focus on the sources of oil and gas in the Z21 structure<sup>16,50</sup>, but no interpretation of occurrences of water in the oil-bearing depth in K22 set was given. Another research published by Liu et al.<sup>14</sup>, successfully interpreted the decreasing current formation pressure coefficients data values from the wells H1D, H1DSa and H18, compared to the original formation pressure coefficient; and the reservoir connectivity between the west zone and main zone (locations of two zones see Figure. 4). However, still no answer was provided to the question that where the water comes from the oil-bearing sandstones.

In this study, a possible schematic pattern for water, oil and gas is proposed based on the sedimentary structures of cores, diagenesis, and physical properties (Figure. 16). As it has been proved that there is a low-permeability belt connecting main zone and the west zone (Figure. 16a)<sup>14</sup>. This is important foundation of the proposed water-oil-gas distribution pattern in this study. The original formation of K22 set is characterized by high water saturation (Figure.16a). As the gas begins to charge, a mass of effective pore spaces was filled with gas; meanwhile, the original formation water was forced to move to the low-pressure area by pore pressure, which is higher than the hydrostatic pressure (Figure.16b and 16c). Local sandstones (e.g., Figure. 5-C and 5-D) with low porosity and permeability were uncharged by gas and the original formation water was left behind, regarding as irreducible water (Figure.16b and 16c). Subsequently, oil begins to charge when the gas accumulation was finished<sup>16</sup> and stops until both oil-water and oil-gas interfaces were formed (Figure. 16d). When wells were drilled in the main zone, the formation pressure of west zone decreases, breaking the preexisting balance state of oil and water, partial irreducible water convert to movable water (Figure. 16e). As the production of the main zone goes on and the drill of well H1D, H1DSa and H18, formation of the west zone decreases severely, resulting in more irreducible water turning into movable water (Figure. 16f).

## Conclusions

A total of 6 depositional lithofacies, Sp, Sm, Sr, Sw, Sl, Fl, and two depositional elements, SB and SS, were identified. The SB was deposited in relatively high-energy hydrodynamic environment, forming better-quality reservoir than SS. The Miocene reservoir in Z21 oil-gas field is dominated by medium-grained sandstones and generally the coarser-grained sandstones are characterized by better reservoir quality than smaller-sized sandstones.

Three main pore types, namely residual primary intergranular pores, secondary dissolution pores and micropores are observed. The deeper sandstones may have higher porosity and permeability values than the shallower sandstones because the former have a greater proportion in secondary dissolution pores.

Mechanical compaction, cementation of calcite and clay mineral cementation are responsible for the porosity and permeability reduction.

Gas and oil in the Z21 structure are characterized by multiple-source supply and the charge of gas occurs prior to oil. The Z21 structure could be regarded as a pool which has a gas cap and oil ring; within the oil ring there exists local irreducible water stored in poor-quality sandstones like lenticular sandstones. This kind of formation water convert to movable water when the formation pressure decreases caused by drill and production activities.

# Declarations

## Acknowledgments

We thank Shenzhen Branch of China National Offshore Oil Corporation (CNOOC) for supply testing data and offering convenience for observing and sampling cores.

## Author Contributions

Conceptualization, methodology and original draft preparation, L.L. & H.D.; formal analysis, review and editing, Z.S.; data curation and investigation; R.F. & R.H.; project administration, resources, J.Z. All authors have read and agreed to the published version of the manuscript.

## Funding

This research was funded by the National Natural Science Foundation of China (No. 42102161) and the Research Foundation for Advanced Talents of Lingnan Normal University (No. ZL1932; ZL2021012).

## Conflicts of Interest

The authors declare no competing interests.

# References

1. Zhou, S. W. *et al.* The current state and future of offshore energy exploration and development technology. *Engineering Sciences*, **18**, 19–31 (2016).
2. Hou, X. L. *The sustainable development of oil and gas resources strategy research report China* (Chinese Academy of Engineering, Beijing, 2005).
3. Xu, S. *et al.* Hydrocarbon migration and accumulation in the northwestern Bohai Bay Basin, China. *J Petrol Sci Eng*, **172**, 477–488 (2019).
4. Zhu, W. L. *et al.* The formation and evolution of the East China Sea Shelf Basin: A new view. *Earth-Sci Rev*, **190**, 89–111 (2019).
5. Tian, J., Hao, F., Zhou, X., Zou, H. & Peng, B. Hydrocarbon generating potential and accumulation contribution of the Fourth member of the Shahejie Formation in the Liaodong Bay sub-basin, Bohai Bay Basin. *Mar Petrol Geol*, **82**, 388–398 (2017).
6. Ye, J. R., Qing, H. R., Bend, S. L. & Gu, H. R. Petroleum systems in the offshore Xihu Basin on the continental shelf of the East China Sea. *AAPG Bull*, **91**, 1167–1188 (2007).
7. Li, S. F. *et al.* Characteristics of Paleogene source rocks and predictions of petroleum resources in Huizhou depression, Pearl River Mouth Basin. *Earth Sci. (J. China Univ. Geosci.)*, **38**, 112–120 (2013).
8. Wei, Q. L., Zheng, R. C., Shi, H. S., Du, J. Y. & Li, X. Y. High resolution sequence stratigraphic characteristics of the Paleogene Zhuhai Formation in Huizhou depression marine delta. *Acta Sedimentol. Sin*, **26**, 744–752 (2008).
9. Zhou, Z. & Wittington, R. J. Tectonic evolution of the Pearl River Mouth Basin, northern South China Sea: abstract. *AAPG Bull*, **78**, 1172 (1994).
10. Ding, N. *et al.* Depositional evolution and genesis of K set of shelf sand ridges in the Zhujiang Formation of Huizhou sag, Pearl River Mouth Basin. *Oil Gas Geol*, **35**, 379–385 (2014).
11. Zhang, J. L., Sun, Z. Q., Liu, L. L. & Li, Y. Sedimentary model of K-Successions Sandstones in H21 Area of Huizhou Depression, Pearl River Mouth Basin, South China Sea. *Open Geosci*, **11**, 97–1013 (2019).
12. Wu, J., Ye, J. R. & Shi, H. S. Reservoir-forming pattern of typical hydrocarbon accumulation zone in Huizhou sag. *Journal of Southwest Petroleum University (Science & Technology Edition)*, **34**, 17–26 (2012).
13. He, M., Huang, Y. P. & Zhu, J. Z. Dynamic evaluation of oil and gas resources in eastern Pearl River Mouth basin. *China Offshore Oil and Gas*, **29**, 1–11 (2017).
14. Liu, L. L. *et al.* Constraints of three-dimensional geological modeling on reservoir connectivity: A case study of the Huizhou depression, Pearl River Mouth basin, South China Sea. *J. Asian Earth Sci*, **171**, 144–161 (2019).
15. Liu, Z. S., Shi, H. S., Yang, S. K., Zhang, M. & Pang, X. The practice of self-operated exploration and its achievements in the eastern South China Sea. *China Offshore Oil and Gas*, **26**, 1–10 (2014).

16. Zhu, M. *et al.* Hydrocarbon origin and favorable progressive exploration area of HZ21-1 structure in Huizhou sag. *China Offshore Oil and Gas*, **29**, 12–22 (2017).
17. Chen, S. & Pei, C. Geology and geochemistry of source rocks of the eastern Pearl River Mouth Basin, South China Sea. *J. Southeast Asian Earth Sci*, **8**, 393–406 (1993).
18. Robison, C. R., Elord, L. W. & Bissada, K. K. Petroleum generation, migration, and entrapment in the Zhu 1 depression, Pearl River Mouth Basin, South China Sea. *Int. J. Coal. Geol*, **37**, 155–178 (1998).
19. Peng, J. W. *et al.* Geochemistry, origin, and accumulation of petroleum in the Eocene Wenchang Formation reservoirs in Pearl River Mouth Basin, South China Sea: a case study of HZ25-7 oil field. *Mar. Petrol. Geol*, **80**, 154–170 (2017).
20. Deng, H. W. & Zheng, W. B. Depositional characteristics of offshore tidal deposits in the lower Tertiary Zhuhai Formation, Huizhou depression, Pearl River Mouth Basin. *Geosci*, **23**, 767–775 (2009).
21. Cheng, T., Wang, Z. Q., Zhang, S. F. & Liu, J. Research on high-resolution sequence stratigraphy of marine-continental alternating facies delta-taking Zhuhai Formation in Huizhou sag, Pearl River Mouth Basin as an example. *Petrol. Geol. Recovery Efficiency*, **14**, 46–51 (2007).
22. Chen, C. M. Petroleum geology and conditions for hydrocarbon accumulation in the eastern Pearl River Mouth Basin. *China Offshore Oil Gas (Geol.)*, **12**, 2–12 (2000).
23. Chen, C. M., Shi, H. S. & Xu, S. C. *The conditions of hydrocarbon accumulation of the Tertiary petroleum system in the Pearl River Mouth Basin* 1st ednpp. 100–101 (Science Press, Beijing, China, 2003).
24. Hu, Y., Hao, F., Zhu, J. Z., Tian, J. Q. & Ji, Y. B. Origin and occurrence of crude oils in the Zhu1 sub-basin, Pearl River Mouth basin, China. *J. Asian Earth Science*, **97**, 24–37 (2015).
25. Folk, R. L. *Petrology of Sedimentary Rocks* (Hemphill Publishing Company, Austin, Texas, 1974).
26. Fon, N. Offshore bar deposits of semilla sandstone member of Mancos Shale (Upper Cretaceous), San Juan Basin, New Mexico. *AAPG Bull*, **65**, 706–721 (1981).
27. Miall, A. D. A review of the braided-river depositional environment. *Earth-Sci. Rev*, **13**, 1–62 (1977).
28. Gani, M. R. & Alam, M. M. Fluvial facies architecture in small-scale river systems in the Upper Dupi Tila Formation, northeast Bengal Basin, Bangladesh. *J. Asian Earth Sci*, **24**, 225–236 (2004).
29. Sharma, M., Sharma, S., Shukla, K. U. & Singh, B. I. Sandstone body architecture and stratigraphic trend in the Middle Siwalik Succession of the Jammu area, India. *J. Asian Earth Sci*, **20**, 817–828 (2002).
30. Roberts, E. M. Facies architecture and depositional environments of the Upper Cretaceous Kaiparowits Formation, southern Utah. *Sediment Geol*, **197**, 207–233 (2007).
31. Wang, Y. F., Wang, Y. M., Li, D., Xu, Q. & Huang, Z. K. Characteristics of reservoirs in the Pearl River Mouth Basin. *Oil Geophysical Prospecting*, **46**, 952–960 (2011).
32. Wu, Y. T. *et al.* Research on sequence stratigraphy of Zhujiang Formation in West Huizhou Sag. *Science Technology and Engineering*, **14**, 111–116 (2014).
33. McGowen, J. H. & Garner, L. E. Physiographic features and stratification types of coarse-grained point bars: modern and ancient examples. *Sedimentology*, **14**, 77–111 (1970).
34. Schmidt, V. & McDonald, D. A. Texture and recognition of secondary porosity in sandstones. *Spec. Publ*, **2**, 209–225 (1979).
35. Craig, F. F. The reservoir engineering aspects of water flooding. *SPE Monograph*, **3**, 63–66 (1972).
36. Gunter, G. W., Pinch, J. J., Finneran, J. M. & Bryant, W. T. Overview of an Integrated Process Model to Develop Petrophysical Based Reservoir Descriptions: SPE California Regional Meeting. Paper 16370 (1997)
37. Zheng, J. M. & Pang, M. *Study on Clastic Diagenesis* 1st ednPP. 110–120 (China University of Geosciences Press, Wuhan, China, 1989).
38. Morad, S., Ketzer, J. M., De Ros, L. F. & Spatial and temporal distribution of diagenetic alterations in siliciclastic rocks: Implications for mass transfer in sedimentary basins. *Sedimentology*, **46**, 95–120 (2000).
39. Wu, J. *Enrichment regularity of Zhu ... Depression, Pearl River Mouth Basin* (China University of Geoscience, Wuhan. (Doctor, 2013).
40. Bjørlykke, K. Relationships between depositional environments, burial history and rock properties. Some principal aspects of diagenetic process in sedimentary basins. *Sediment. Geol*, **301**, 1–14 (2014).
41. Hendry, J. P. & Trewin, N. H. Authigenic quartz microfabrics in Cretaceous turbidites, evidence for silica transformation processes in sandstones. *J Sediment Res*, **65**, 380–392 (1995).

42. Worden, R. H. & Morad, S. Clay minerals in sandstones: Controls on formation, distribution and evolution. In: Worden, R.H., Morad, S. (Eds.), *Clay Mineral Cements in Sandstones*, 34. International Association of Sedimentologists Special Publications. pp. 3–41 (2003)
43. Wang, G. W., Chang, X. C., Yin, W., Li, Y. & Song, T. T. Impact of diagenesis on reservoir quality and heterogeneity of the Upper Triassic Chang 8 tight oil sandstones in the Zhenjing area, Ordos Basin, China. *Mar. Petrol. Geol.*, **83**, 84–96 (2017).
44. Ehrenberg, S. N. & Nadeau, P. H. Formation of diagenetic illite in sandstones of the Garn Formation, Haltenbanken area, mid-Norwegian continental shelf. *Clay Miner.*, **24**, 233–253 (1989).
45. Hellevang, H., Aagaard, P., Oelkers, E. H. & Kvamme, B. Can dawsonite permanently trap CO<sub>2</sub>? *Environ. Sci. Technol.*, **39**, 8281–8287 (2005).
46. Liu, L. L., Li, Y., Dong, H. Z. & Sun, Z. Q. Diagenesis and reservoir quality of Paleocene tight sandstones, Lishui Sag, East China Sea Shelf Basin. *J Petrol Sci Eng.*, **195**, 107615 (2020).
47. Xiang, F. D. Carbon dioxide reservoir and its significance to hydrocarbon accumulation in eastern Pearl River Mouth Basin. *China Offshore Oil and Gas (Geology)*, **8**, 155–162 (1994).
48. Zhao, S., Du, J. F., Liu, L. & Yu, Z. C. Characteristics of authigenic minerals and paragenetic sequence of dawsonite-bearing sandstones from the Mingyuefeng Formation of Paleocene in Lishui Sag, East China Sea Basin. *J. Mineral Petrol.*, **33**, 85–93 (2013).
49. Zhao, S., Liu, L. & Liu, N. Petrographic and stable isotopic evidence of CO<sub>2</sub>-induced alterations in sandstones in the Lishui sag, East China Sea Basin, China. *Appl. Geochem.*, **90**, 115–128 (2018).
50. Zhu, M. *et al.* Geological characteristics and accumulation mechanism of Paleocene reservoir in Huizhou sag, Pearl River Mouth basin. *China Offshore Oil and Gas*, **29**, 1–11 (2017).
51. Liu, L. L., Zhang, J. L., Sun, Z. Q. & Yu, T. Diagenesis of Chang6 Formation of Hu2 block, Huanjiang oilfield, Ordos Basin. *Petrol Sci Technol.*, **35**, 1–7 (2017).
52. Li, Y., Chang, X. C., Yin, W., Sun, T. T. & Song, T. T. Quantitative impact of diagenesis on reservoir quality of the Triassic Chang 6 tight oil sandstones, Zhenjing area, Ordos Basin, China. *Mar. Petrol. Geol.*, **86**, 1014–1028 (2017).
53. Worden, R. H., Mayall, M. & Evans, I. J. The effect of ductile-lithic sand grains and quartz cement on porosity and permeability in Oligocene and lower Miocene clastics, South China Sea: prediction of reservoir quality. *AAPG Bull.*, **84**, 345–359 (2000).
54. Houseknecht, D. W. Assessing the relative importance of compaction processes and cementation to reduction of porosity in sandstones. *AAPG Bull.*, **71**, 501–510 (1987).
55. Bjorlykke, K. Relationships between depositional environments, burial history and rock properties. Some principal aspects of diagenetic process in sedimentary basins. *Sediment Geol.*, **301**, 1–14 (2014).
56. Umar, M., Friis, H., Khan, A. S., Kassi, A. M. & Kasi, A. K. The effects of diagenesis on the reservoir characters in sandstones of the late Cretaceous Pab formation, Kirthar fold belt, southern Pakistan. *J. Asian Earth Sci.*, **40**, 622–635 (2011).
57. Giles, M. R. & De Boer, R. B. Origin and significance of redistributional secondary porosity. *Mar. Petrol. Geol.*, **7**, 378–397 (1990).
58. Bjorlykke, K. & Jahren, J. Open or closed geochemical systems during diagenesis in sedimentary basins: Constraints on mass transfer during diagenesis and the prediction of porosity in sandstone and carbonate reservoirs. *AAPG Bull.*, **96**, 2193–2214 (2012).

## Figures

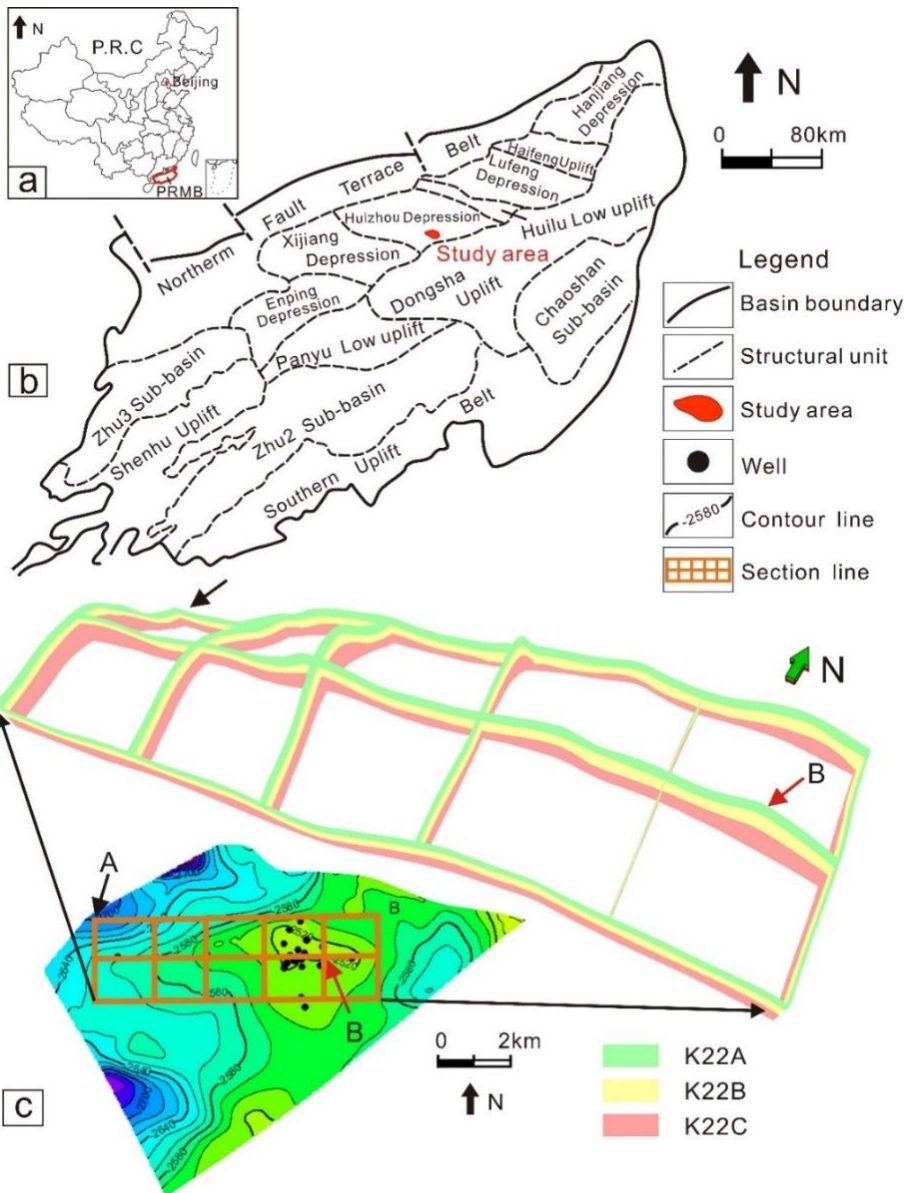


**Figure 1**

(a) Map of the People's Republic of China and location of the PRMB. (b) Structural map of the PRMB, showing different sub-structural units in the basin. (c) Three-dimensional fence diagram of the studied strata. A refers to a structural low, B refers to a structural high. K22A, K22B and K22C are three subdivided layers from K22 layer. The red arrows refer to the structural high, the black arrow refers to the structural low.

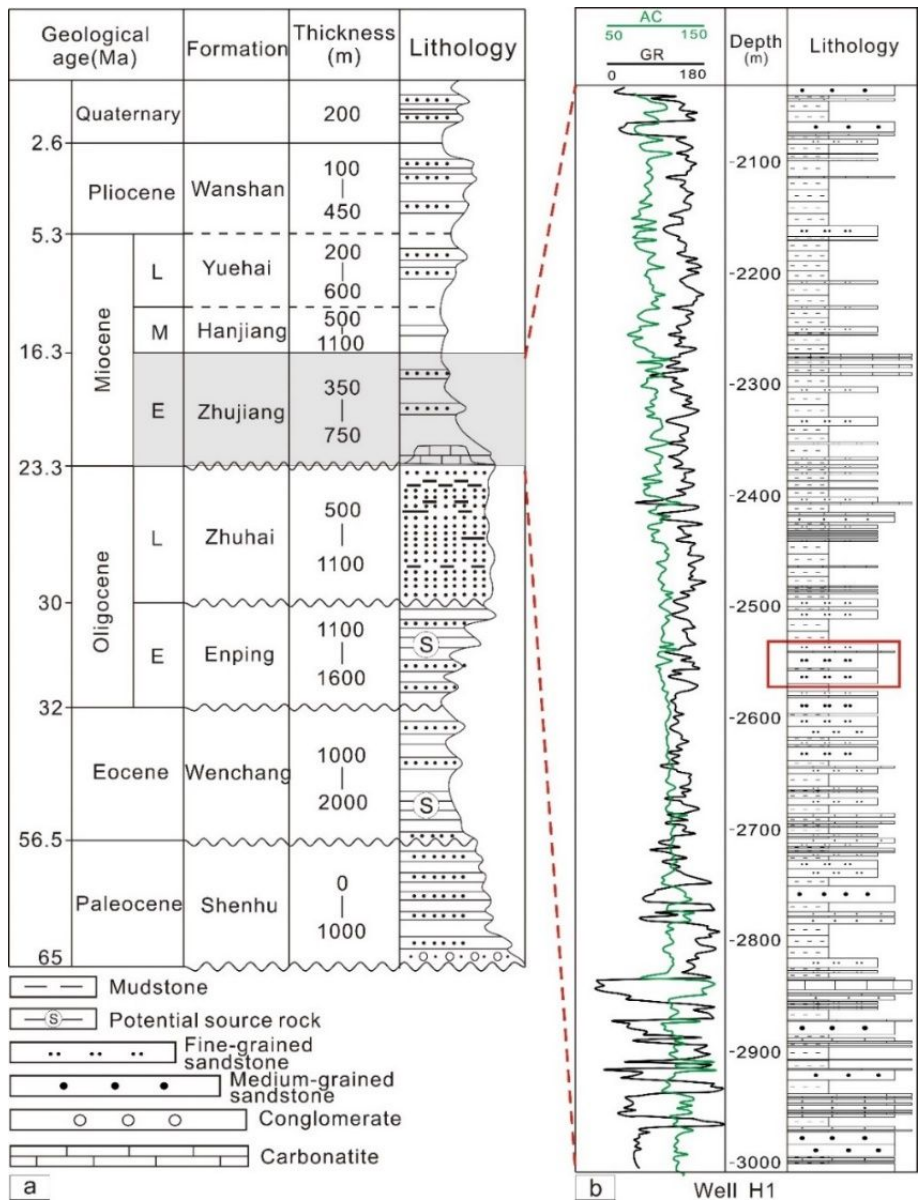


**Figure 2**

(a) Stratigraphic units of the PRMB (Modified after Chen and Pei17and Robison et al.18). (b) Detailed stratigraphic column of well H1. The K22 layer is shown in the red box14.

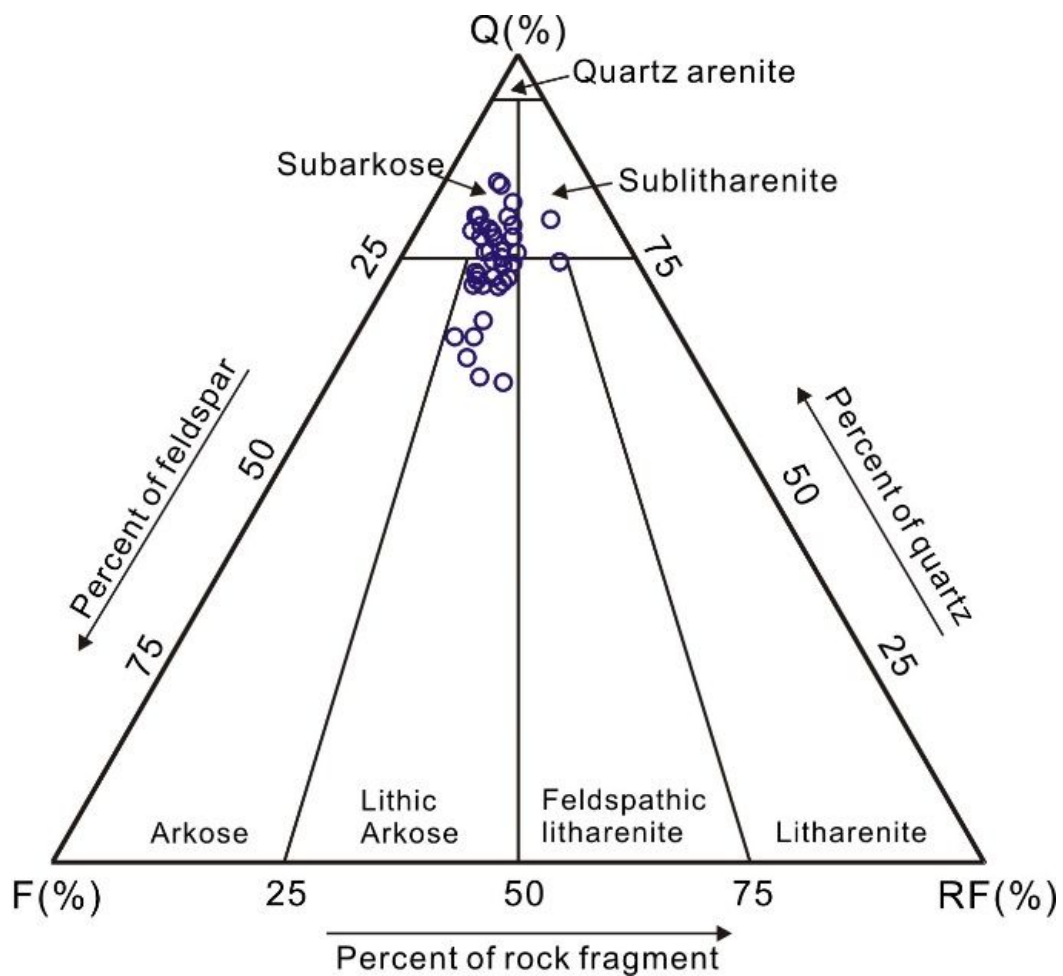
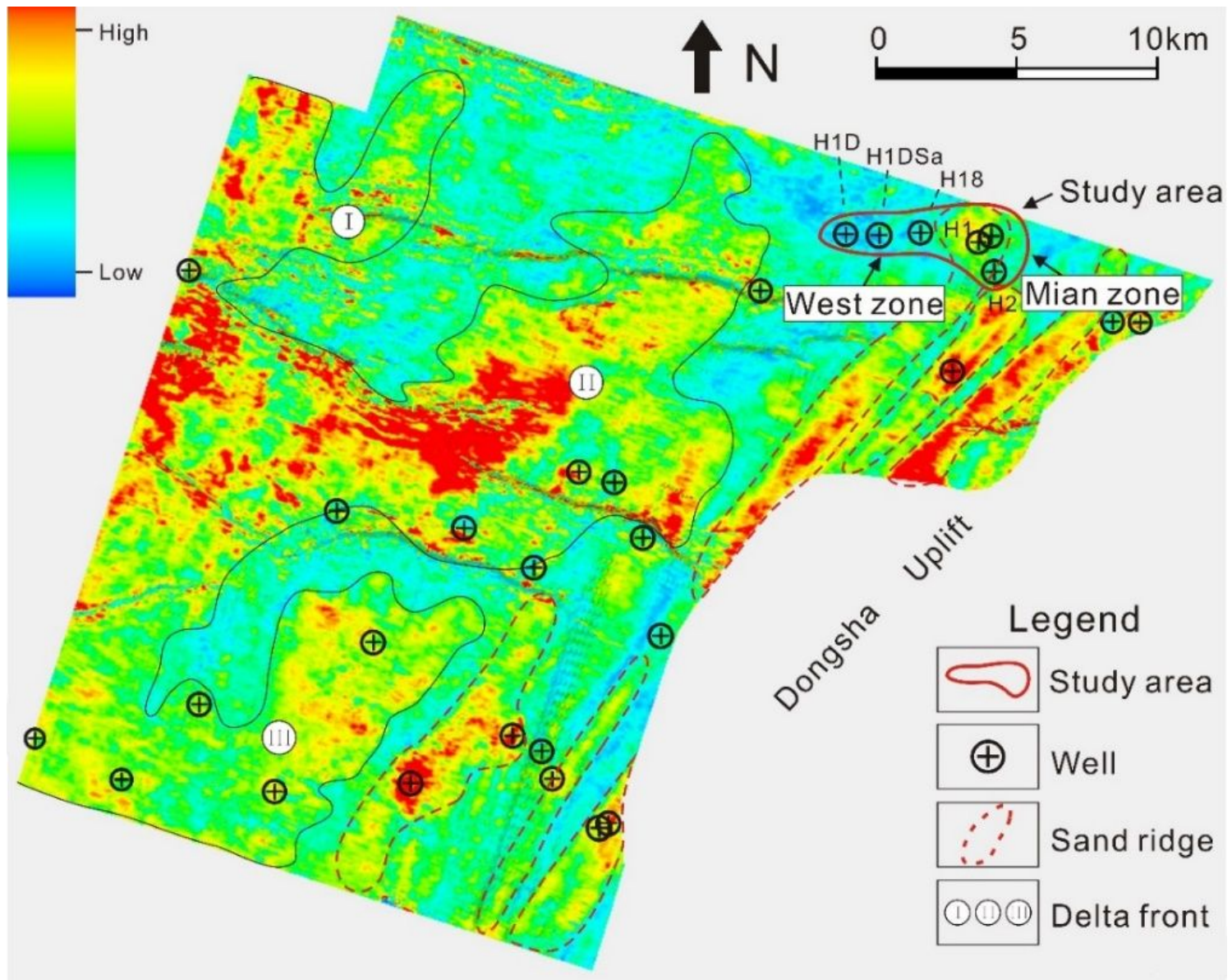


Figure 3

Ternary diagram exhibiting the framework grain composition of the Miocene Zhujiang Formation in Z21 oil-gas field in Huizhou depression. Q=quartz, F=feldspar, RF=rock fragments.



**Figure 4**

Seismic distribution model sandstone and mudstone of K22 layer, obtained from geostatistical inversion (After CNOOC)14. This inversion profile is based on high-resolution seismic data and logging data.

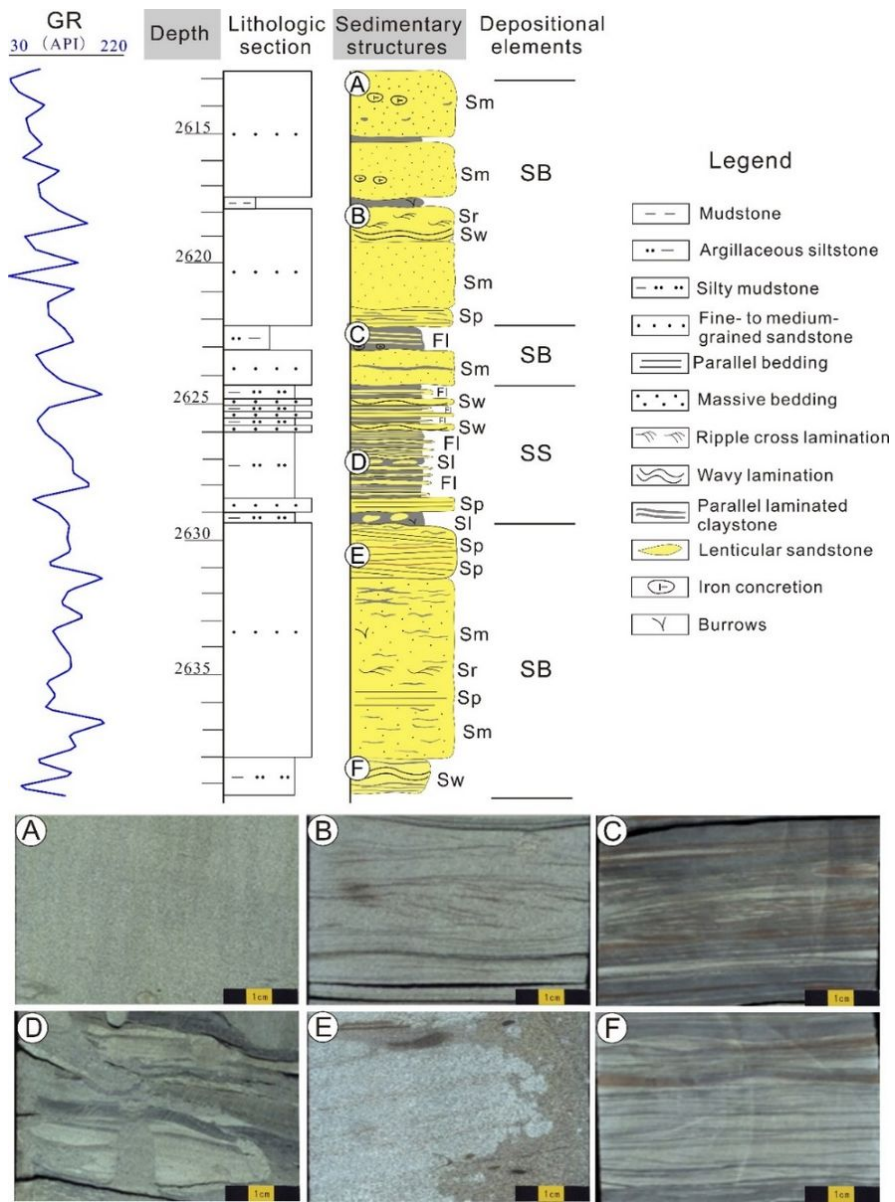


**Figure 5**

Single well section description of well H2. Sm, SP, Sr, SI, Sw and FI represent 6 different lithofacies. SB and SS represent 2 different depositional elements. See detailed information of these acronyms in the text.

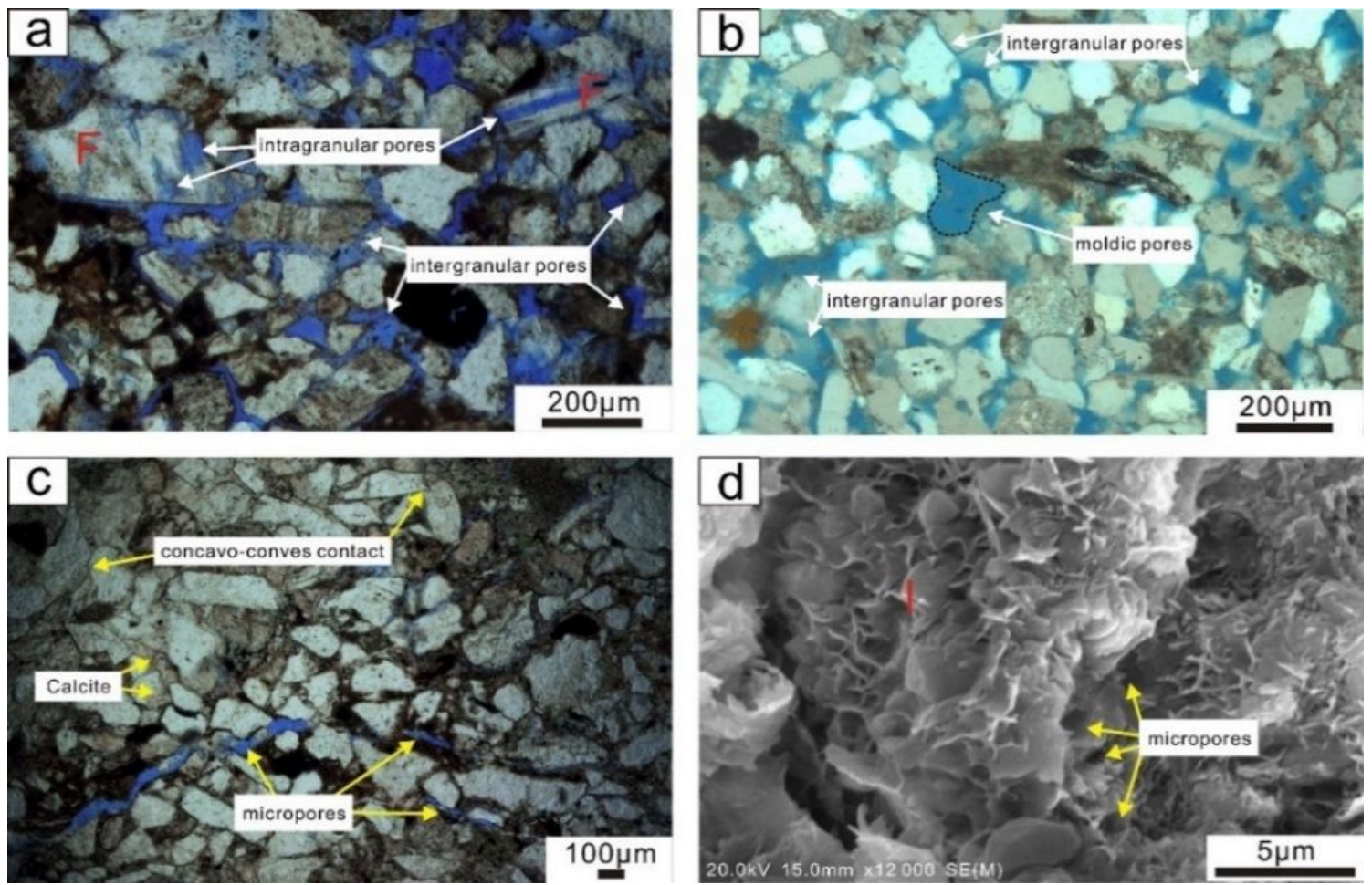


Figure 6

Thin section photomicrographs and SEM images showing details of grain and pore modifications. (a) Primary intergranular pores and secondary dissolution intragranular pores resulting from dissolution of feldspars under the microscope, well H2, 2436.6m, plane-polarized light (PPL); (b) Primary intergranular pores and moldic pores resulting from complete dissolution of grains, in well H3, 2702.82 m, PPL. (c) Micro-fractures distributed between directionally arranged grains, concavo-conves contact are frequent in this view, well H2, 2433.85m, PPL; (d) Intercrystalline micropores within honeycomb-like illite cements, widths of this types of micropores are usually less than 5µm, well H4, 2621.5m, SEM. F=feldspar, I=illite.

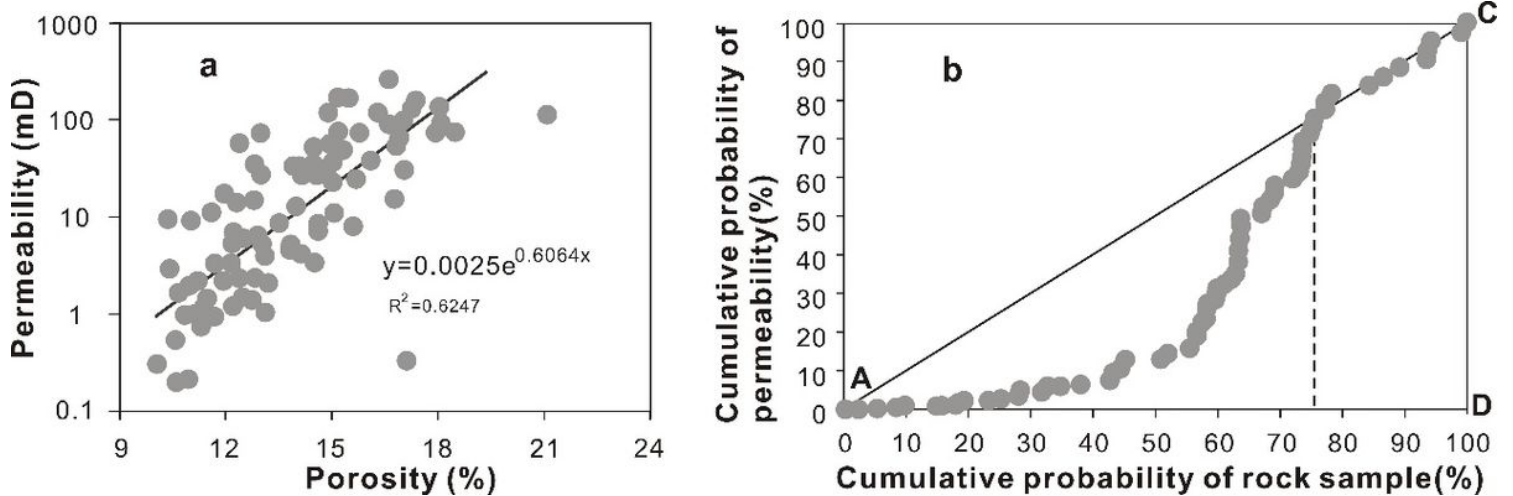
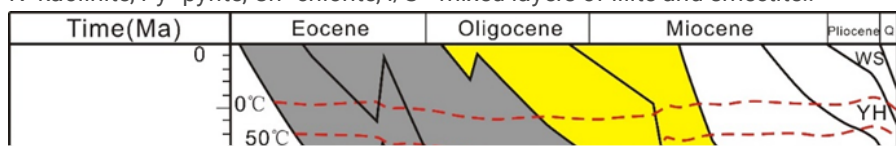


Figure 7

(a) Relationship between porosity and permeability values. (b) Lorenz plot of permeability of K22 set in Z21 oil-gas field. Strong reservoir heterogeneity is indicated by this figure.

**Figure 8**

Optical thin sections and SEM images showing (a) directional arrangement of framework grains caused by mechanical compaction, approximately in the direction shown by the blue arrow, well H4, 2530.5m, PPL; (b) deformed rock fragment, probably micas, well H3, 2560.8m, SEM; (c) authigenic quartz cements adjacent to dissolved feldspar with obvious intragranular pores (pointed by a green arrow), well H2, 2536.6m, SEM; (d) vermiform kaolinite accompanied by the coprecipitation of calcite in the primary residual intergranular pores, well H3, 2702.8m, SEM; (e) fibrous illite, partially converting into smectite, intercrystalline micropores are rare, well H4, 2720.5m, SEM; (f) Calcite cements completely occlude the intergranular pores, well H1, 2533.8m, cross-polarized light; (g) Fibrous dawsonite, well H1, 2579.9m, SEM; (h) frambooidal aggregates of pyrite accompanied by illite and quartz overgrowth, well H2, 2582.5m, SEM; (i) flaky chlorite growth on the edge of the quartz overgrowth, well H2, 2979m, SEM; (j) dissolution of feldspar, producing intragranular pores (green arrows), well H2, 2582.5m, SEM. Qa=authigenic quartz, Qo=overgrowth, Cal=calcite, Daw=dawsonite, Mi=mica, F=feldspar, I=illite, K=kaolinite, Py=pyrite, Ch=chlorite, I/S= mixed layers of illite and smectite..



**Figure 9**

Burial-thermal history of Well H1 and the paragenetic sequence and types of diagenesis in the Miocene Zhuijiang Formation sandstones39, 50. Q=Quaternary.

**Figure 10**

Statistics of porosity and permeability of different depositional elements (a) and different grain-sized sandstones (b).

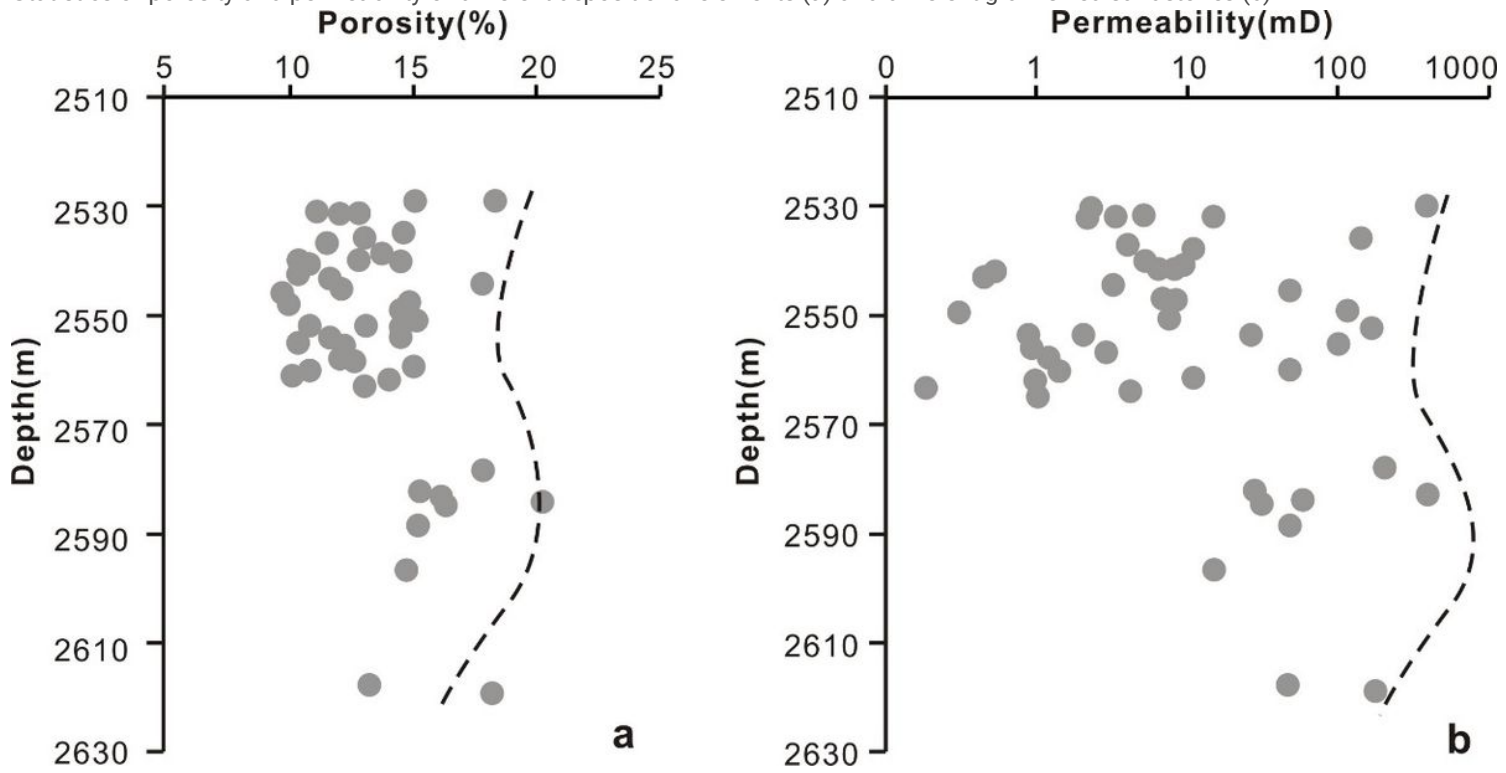


**Figure 11**

Plot of the depth versus porosity (a) and permeability (b) for the Miocene ZJ Formation sandstones of Z21 gas field in Huizhou Depression.

**Figure 12**

Plot of the calcite versus porosity (a) and permeability (b) for the Miocene ZJ Formation sandstones of Z21 oil-gas field field in Huizhou Depression.

**Figure 13**

Variations in the content of kaolinite (a and b), illite (c and d), chlorite (e and f) and total content of clay minerals (g and h) with the porosity and permeability values

**Figure 14**

Tendency chart between pore proportion and porosity/permeability values of certain samples.

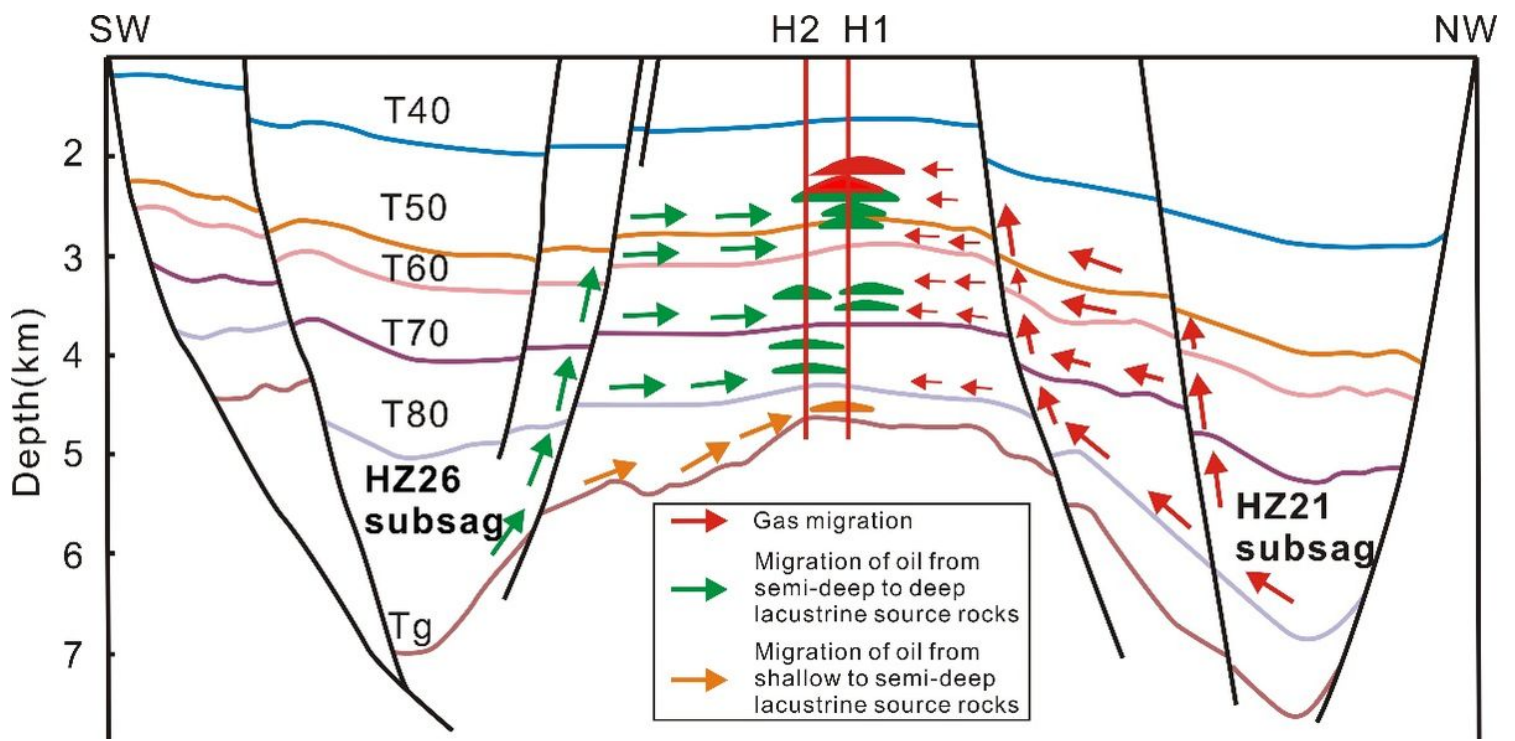


Figure 15

Hydrocarbon accumulation mode in Z21 structure16.

